Investigation of Active Rotor Design and Control for Performance Improvement

Dominik Komp Research Assistant
Sumeet Kumar Research Assistant
Amine Abdelmoula Research Assistant
Manfred Hajek Full Professor
Jürgen Rauleder Lecturer

Institute of Helicopter Technology, Technical University of Munich
Munich, Germany

Abstract

A computational investigation was conducted to identify the optimal performance of a rotor with an active camber morphing mechanism using up to twice-per-revolution (2P) control input. Using rotor comprehensive analysis with an elastic blade model and a free vortex wake for the aerodynamics model to ensure computational efficiency, a parametric study of design and control variables was carried out to identify their influence on rotor performance. The same computational framework was used to obtain optimal control inputs that led to best performance using 2P individual blade control (IBC) via pitch-link inputs and 2P active twist control. The relative potential of the three active mechanisms to improve rotor performance was studied and compared. A level flight condition at $\mu = 0.3$ and $C_T/\sigma = 0.089$ was used throughout this investigation. IBC or active twist both yielded maximum performance improvements of 1.8% in terms of power reduction. Optimal isolated 1P and 2P active camber actuation resulted in performance improvements of 3.6% and 3.1%, respectively. Using the best combination of geometric design and optimal superimposed 1P+2P actuation, a rotor power reduction of 4.4% was obtained. Overall, the rotor performance gains obtained using each active rotor mechanism that was investigated were attributed to a more uniform distribution of thrust over the rotor disk.

Notation

α	blade section angle of attack, deg
α_s	rotor shaft tilt (negative forward), deg
Δ	denoting change in quantities compared to baseline results
δ	active camber deflection (positive downwards), deg
δ_0	mean active camber deflection during actuation cycle, deg
$\delta_{\min}$	minimum active camber deflection during actuation cycle, deg
μ	advance ratio, $V_\infty/\Omega R$
Ω	angular velocity of rotor blade, rad/s
ω	blade frequency, rad/s
$\phi_{n\mathrm{P}}$	phase of nP active actuation input, deg
ψ	rotor azimuth (counter-clockwise), deg
ρ	density of air, $\mathrm{kg/m^3}$
σ	rotor solidity, $Nc/\pi R$
θ	blade pitch angle at the root, deg
θ_0	rotor collective pitch angle, deg
θ_{1s}, θ_{1c}	rotor cyclic pitch angles, deg
θ_{atw}	blade active twist input (higher negative value implies greater twist), deg
θ_{IBC}	IBC blade pitch input, deg
θ_{tw}	induced elastic blade twist (higher negative value implies greater twist), deg
$A_{n\mathrm{P}}$	amplitude of nP active actuation, deg
c	blade chord, m
C_d	2-D airfoil drag coefficient
C_H	drag force coefficient (shaft axis), $H/\pi\rho R^2(\Omega R)^2$
C_l	2-D airfoil lift coefficient
C_m	2-D airfoil moment coefficient
C_P	rotor power coefficient, $P/\pi\rho R^2(\Omega R)^3$
C_T	rotor thrust coefficient (shaft axis), $T/\pi\rho R^2(\Omega R)^2$
C_{M_x}	roll moment coefficient (shaft axis), $M_x/\pi\rho R^3(\Omega R)^2$
L/D_e	rotor lift-to-equivalent-drag ratio
M	relative oncoming flow Mach number
M_x	hub roll moment (shaft axis, right wing up positive), Nm
N	number of rotor blades
n	active control input harmonic (1/rev)
P_{ind}	section induced power, N/s
P_{prof}	section profile power, N/s
R	rotor disk radius, m
r	radial position of the active camber section center normalized by rotor radius
s	spanwise length of the active camber section normalized by rotor radius

Presented at the Vertical Flight Society 75th Annual Forum & Technology Display, Philadelphia, Pennsylvania, May 13–16, 2019.

Introduction

The conventional static rotor design poses several performance limitations. These limitations are due to the different flow conditions experienced over different sections of the rotor disk. In the past, different mechanisms have been pro-

posed and studied to ameliorate the shortcomings of a static rotor design. For example, full-blade feathering systems for higher harmonic pitch control via the swashplate or through actuators in the blade pitch links, and a multitude of active morphing sections on rotor blades have been investigated.

Investigations into the use of trailing-edge flaps (TEFs) on rotor blades have reported performance gains for higher harmonic flap deflections with appropriate phasing over the rotor azimuth (Refs. 1–5). Jain et al. (Ref. 2) used a comprehensive analysis with free wake modeling to simulate a UH-60A helicopter with TEF in forward flight at $\mu = 0.368$ and $C_T/\sigma = 0.084$. Increments in rotor L/D_e of 7.6% and 4.4% were obtained using TEF actuation at 1P and 2P, respectively. At 1P actuation, performance gains were obtained when peak positive (downward) flap deflection occurred in a limited azimuth range about $\psi = 90^\circ$, leading to increased disk loading on the rotor advancing side with little effect on disk loading elsewhere. 2P actuation yielded performance gains when peak positive flap deflection occurred at the front and aft sections of the rotor disk. This flap actuation profile causes a positive pitch-up moment on the advancing side, increasing the angles of attack near the blade tip region and, consequently, increasing the blade loading there. Ravichandran et al. (Ref. 4) also simulated the UH-60A helicopter at lower C_T/σ =0.0783 and reported similar effects of optimal 2P harmonic TEF actuation on rotor performance.

Full-scale Bo 105 rotor tests were conducted in the NASA Ames 40-by-80-foot wind tunnel to measure the effect of 2P individual blade control (IBC) input through the pitch link on rotor performance (Ref. 6). It was envisioned that for test cases involving high-speed forward flight, optimum 2P IBC input would reduce stall on the retreating side and the high profile losses on the advancing side, improving overall rotor performance. However, no performance gain was measured for $\mu = 0.3$ over a phase sweep of IBC input. At $\mu = 0.4$ and IBC input of 1.0° amplitude, the required power was decreased by 4% for IBC input with a phase of about 100°. This indicates a loading redistribution from the front and aft sections to the lateral sides of the rotor disk. It was concluded that the rotor did not go through dynamic stall since no unusually high vibratory control loads were measured. Therefore, the performance gain observed could not be ascribed to stall alleviation. Full-scale UH-60A rotor tests in the same wind tunnel at $\mu = 0.35$ and 0.4 also showed performance gains with IBC input phase close to 110° suggesting that the same underlying physical effect of loading redistribution was the cause for performance gain (Ref. 7).

Cheng and Celi (Ref. 8) used a rigid blade structural model and linear inflow aerodynamics to examine the effect of 2P IBC input on performance of a UH-60 Blackhawk in free flight. The amplitude of 2P input was maintained at 1° throughout the investigation and a parametric sweep of the input phase delay was carried out. Two different blade loadings, $C_T/\sigma = 0.073$ and 0.099, were studied and optimal performance gains of 1.98% and 11.3%, respectively, were reported. For $C_T/\sigma = 0.073$, the greatest performance gain occurred at a phase angle of 106° with the underlying physical mechanisms, that lead to this improvement, consistent with those reported in the aforementioned studies. However, for $C_T/\sigma = 0.099$, a phase angle of 40° gave the best performance improvement. A refined analysis showed that improved fidelity free wake analysis or structural analysis accounting for blade flexibility only affected the magnitude of performance gain and not the IBC pitch input phase angle. However, the study left scope for improvement since the investigation did not involve free wake inflow simultaneously with a flexible rotor model, and only the phase of optimal input was investigated in this parametric study (Ref. 8).

Numerical simulations of a full-scale UH-60A with active twist in Ref. 2 showed similar performance trends as those obtained for the full-scale rotor using IBC in the wind tunnel (Ref. 7). Jain et al. (Ref. 2) used CFD-CSD coupled analysis to show that, using a 2P active twist scheduling with maximum outboard blade pitch increase of 4° occurring at $\psi = 90^\circ$, a power reduction of 3.3% was possible. Yeo (Ref. 1) also made similar conclusions based on comprehensive analysis of a UH-60A rotor with active twist.

Conclusions from the aforementioned active rotor investigations suggest that the overall rotor aerodynamic effects of IBC, active twist and TEF, manifest in similar ways, even though they affect the blade aerodynamics differently upon actuation. For example, actuating a TEF changes the blade section aerodynamic characteristics of lift, drag, and moment, while active twist and IBC do not. In principle, optimal IBC input introduces a high-frequency blade twist similar to the active twist concept. However, IBC wind tunnel tests of the Bo 105 (Refs. 6, 9) showed that due to blade torsional flexibility the magnitude of the high-frequency pitch inputs at the blade root was only partially transferred to the blade tip, and with a phase delay. The magnitude of this delay in tip twist response depended on the control input harmonics. In contrast, active twist does not inhabit such complex aeromechanical couplings and operates by feathering the blade directly over the span where the mechanism is installed.

Woods et al. (Ref. 10) have demonstrated the feasibility of the Fish Bone Active Camber (FishBAC) concept, as an alternative to TEF, to deform the camber smoothly in the aft section of an airfoil. Based on 2-D wind tunnel tests, the FishBAC mechanism was demonstrated to be aerodynamically more efficient compared to an airfoil with an equivalent size trailing-edge flap because of a more streamlined, continuous profile. Furthermore, using CFD-CSD coupled analysis Jain et al. (Ref. 11) showed that chordwise gaps between the flap and the airfoil all but erase any performance gain. Therefore, for active rotor application an active camber mechanism will be more suitable than a TEF. A previous limited-scope investigation of a rotor with active camber morphing using lower-order modeling showed that it can be used to improve performance both in hover and in forward flight (Ref. 12).

The current study focuses on investigating the relative abilities of three active rotor mechanisms – IBC via pitch-link actuators, active twist, and active camber – to effect a gain

in performance during high-speed forward flight conditions. The underlying aeroelastic effects that lead to optimal performance are contrasted among the three active mechanisms for better insight into their operational differences. A parametric study of critical geometric and control variables relevant to each mechanism is conducted to arrive at optimal designs that yield best performance.

Modeling Approach

The rotorcraft comprehensive analysis tool CAMRAD II (Ref. 13) was used for the current investigation. CAMRAD II is a multi-body dynamics, finite element code for comprehensive rotorcraft analysis with sufficient flexibility to model the true geometry of a rotor system. The full-scale Bo 105 hingeless rotor was used as the baseline to analyze performance gains accrued by means of a morphing camber concept, IBC, and active twist.

Implementation of the Active Rotor Concepts

Figure 1 illustrates the design definitions used during the parametric sweep study of the active camber mechanism. Figure 1a specifies the deflection angle δ as the metric for measuring camber deflection. The baseline (static) airfoil was a NACA23012 and only the aft 25% of the chord were actively morphed. In Figure 1b, variables defining the camber deflection during the actuation cycle (see Eq. 1) are explained. Therein, the positions marked with (b) and (d) represent the limits of actuation. Figure 1c illustrates the parameters r and s, that define the blade section where the active camber mechanism was integrated.

$$\delta = \underbrace{\delta_{\min} + \sum_{n=1}^{2} A_{\mathrm{nP}}}_{\delta_0} + \sum_{n=1}^{2} A_{\mathrm{nP}} \cdot cos(n(\psi - \phi_{\mathrm{nP}})) \qquad (1)$$

Active twist was implemented in CAMRAD II by applying a torsional moment couple at the ends of the active twist morphing section (inboard at $0.25R$, outboard at $0.95R$). IBC was modeled as harmonic input to a pitch link actuator. The corresponding definition of the actuation profile is given in Eqs. 2 and 3. Actuation power required to enable the respective deflections was not considered for any of these concepts.

$$\theta_{\mathrm{IBC}} = A_{\mathrm{nP}} \cdot cos(n(\psi - \phi_{\mathrm{nP}})) \qquad (2)$$

$$\theta_{\mathrm{atw}} = -A_{\mathrm{nP}} \cdot cos(n(\psi - \phi_{\mathrm{nP}})) \qquad (3)$$

Structural Model

A structural model of the full-scale isolated Bo 105 rotor was developed including a swashplate control mechanism. The radial distribution of structural properties of the blade were provided by DLR and were defined at 41 radial stations. The elastic blade motion was calculated using elastic beam theory. Each blade was modeled using seven elastic beam elements

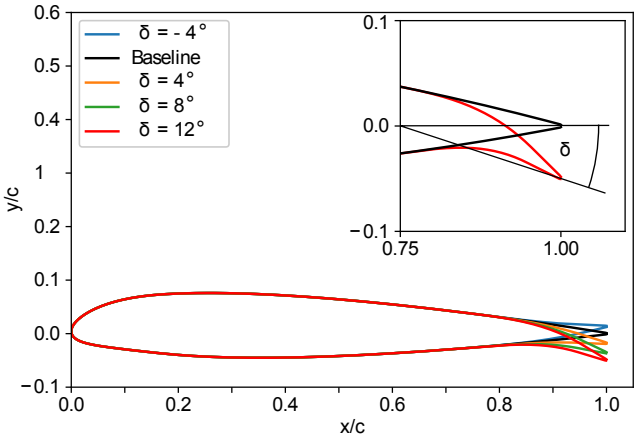

(a) Active camber profiles and δ definition

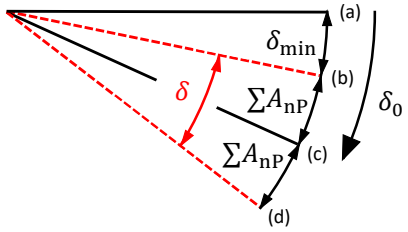

(b) Active camber deflection definition, (a) baseline, (b) minimum deflection, (c) mean active camber deflection, (d) maximum deflection

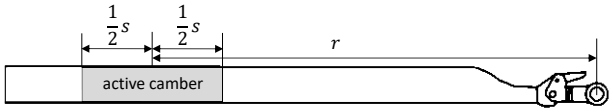

(c) Active camber design parameters

Fig. 1. Geometric definitions for the active camber concept.

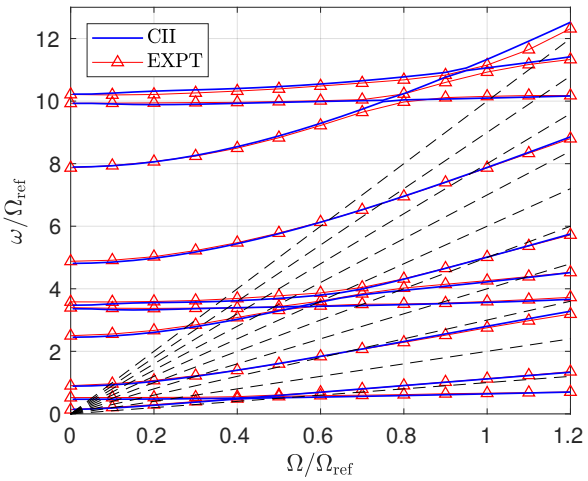

Fig. 2. Baseline fan diagram, comparison for first ten blade modes, $\Omega_{\mathrm{ref}} = 44.4$ rad/s.

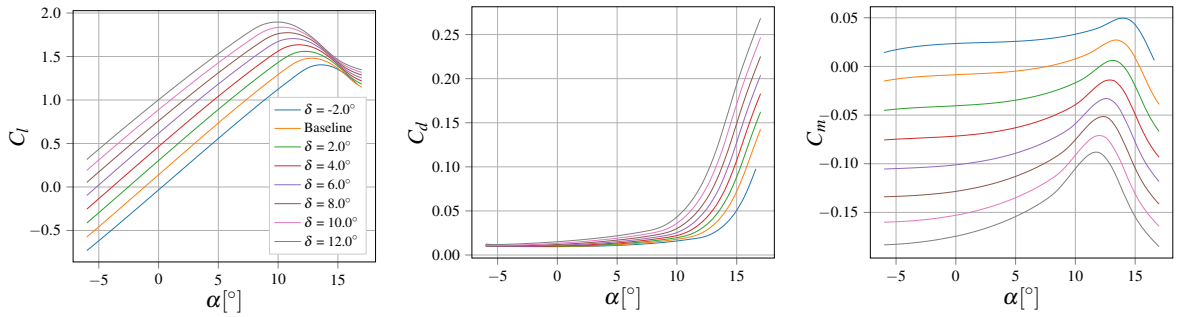

(a) C_l over α (b) C_d over α (c) C_m over α

Fig. 3. The 2-D aerodynamic characteristics of the baseline and camber morphed airfoils at $M = 0.4$.

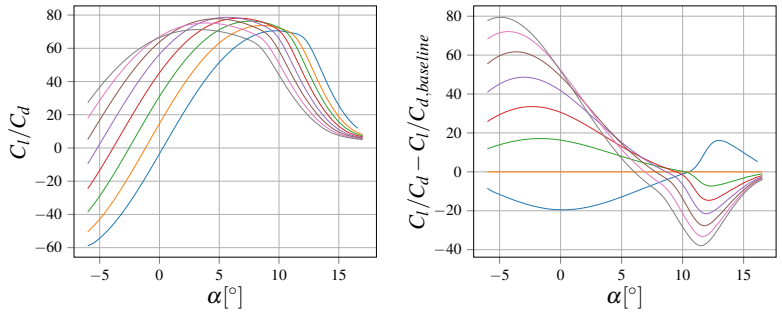

(a) C_l/C_d over α (b) $C_l/C_d - C_l/C_{d,\text{baseline}}$ over α

Fig. 4. Aerodynamic performance of the baseline and the camber morphed profiles at $M = 0.4$.

along the blade span, with six rigid and eight elastic degrees of freedom per element. A comparison of the modal analysis of the CAMRAD II model with DLR reference data showed good agreement (see Fig. 2). The deflection of the active camber section was prescribed. Inertial effects due to dynamic actuation as well as chordwise section deformation were not considered. For the spanwise section of the active camber mechanism, the baseline rotor blade structural properties were assumed.

Aerodynamics Model

In order to accomplish the 3-D comprehensive analysis for an active rotor, the 2-D coefficients, C_l, C_d, and C_m are required for the lifting line theory based analysis. CAMRAD II reads these aerodynamic coefficients as C81 table that includes an angle of attack range of $-180^\circ \leq \alpha \leq 180^\circ$ and Mach number range of $0 \leq M \leq 1$. For the operational regime of the Bo 105 rotor blade that corresponds to a Mach number range of $M = 0.2 - 0.8$ and angle of attack range of $\alpha = -10^\circ - 18^\circ$, the airfoil tables of the baseline NACA23012 and the morphed camber airfoils were generated using the TAU CFD solver (Ref. 14). The Reynolds-averaged Navier–Stokes (RANS) simulations were conducted using the Spalart–Allmaras (SA) turbulence model for turbulence closure. For higher angles of attack, a URANS solver was used for specific cases, since the flow became heavily unsteady. In a previous investigation (Ref. 15), the numerical setup used for the baseline airfoil was validated by experimental data. The morphed profile CFD computations used the same numerical setup (including the meshes) and they were verified by results obtained from MSES.

Figures 3 and Figure 4 show the computed aerodynamic coefficients of the baseline airfoil in comparison to the morphed camber profiles for $M = 0.4$. Although this instance is only for one Mach number, it illustrates how significantly the 2-D aerodynamics change when actuating the active camber mechanism. Note that α was defined as the angle between the unchanged chord line (not taking into account the deflection of the trailing edge) relative to the horizontal (wind) axis for all airfoil shapes. For $M = 0.4$ the best aerodynamic performance was obtained with a moderate increase in camber ($\delta = 4^\circ$ and $\delta = 6^\circ$) and over $\alpha = 3^\circ - 8^\circ$. Negative camber deflection did not improve the airfoil efficiency in the relevant angle of attack region. For the full investigation on the 2-D aerodynamics of active camber see Ref. 15.

These 2-D airfoil characteristics were used in CAMRAD II as look-up tables for the baseline profile NACA23012 and for each deflection. In spanwise direction, the blade was discretized using 28 aerodynamic panels, distributed non-uniformly over the blade. All analyses were carried out using 24 azimuthal stations per revolution, i.e., an azimuthal step size of $\Delta\psi = 15^\circ$. The rotor wake was calculated using a four-trailer free vortex wake analysis with two trailers enframing the aerodynamically active part of the rotor blade,

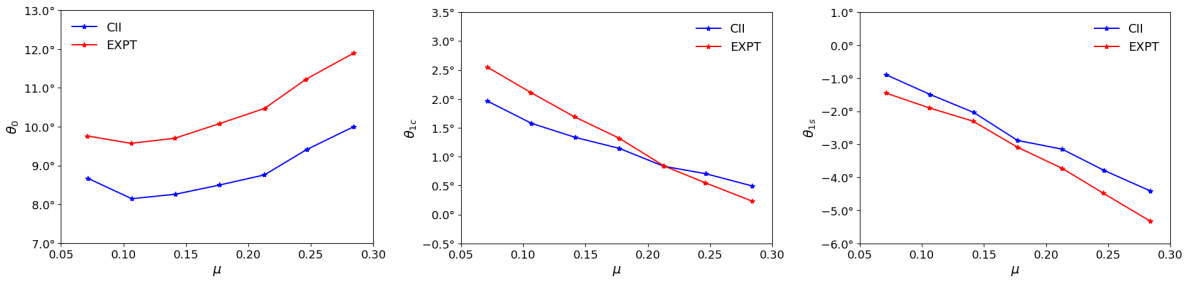

(a) Collective pitch (b) Lateral cyclic (c) Longitudinal cyclic

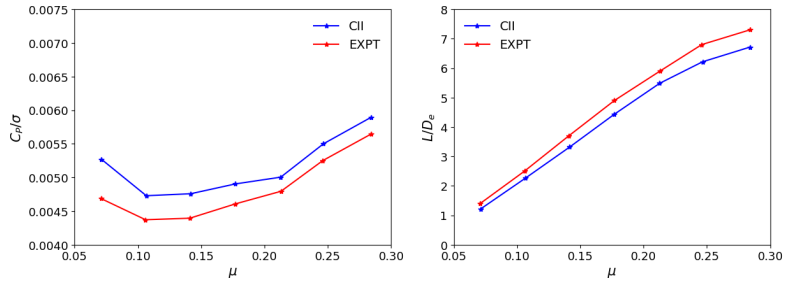

(d) C_P/σ (e) L/D_e

Fig. 5. Correlation of measurement data (EXPT) with CAMRAD II (CII) results for advance ratio sweep at $\alpha_s = -7.5°$, and prescribed thrust and hub moments from Table 1.

at the most inboard ($0.22R$) and outboard ($1.00R$) radial stations. The remaining two trailers enframed the active camber blade section where the morphing concept was implemented. A full wake distortion was computed and vortex roll-up was modeled without consolidation of trailers. The wake geometry was truncated after five revolutions. A single-peak model was used to determine the bound vorticity at the rotor blade. The inboard wake and tip vortices were modeled using the Bagai–Leishman vorticity distribution and core radius growth models (Ref. 16).

Trim Condition: Validation and Active Rotor Study

The trim conditions used for model validation and active rotor study are detailed in Table 1. For validation, the trim condition was based on wind tunnel test data from Ref. 17. In the active rotor study, a propulsive trim was used corresponding to a fast forward flight condition of a Bo 105 free flight test campaign (Ref. 18). Therefore, the rotor physics were representative of a realistic flight condition. Since active rotor inputs affected the rotor aerodynamics, the rotor was re-trimmed for investigations involving active mechanisms to match the trim targets detailed in Table 1.

Table 1. Trim conditions.

Validation	Active rotor study
$\alpha_s = -7.5°$	$\alpha_s = -6.0°$
$\mu = 0.3$	$\mu = 0.3$
$C_T/\sigma = 0.08836$	$C_T/\sigma = 0.089$
$M_x = 253$ Nm	$M_x = 1000$ Nm
$C_H/\sigma = -0.001238$	$C_H/\sigma = 0.000$

Validation

The CAMRAD II model of the isolated Bo 105 rotor was validated using forward flight test conditions from Table 1. The validation was carried out using data available in the open literature from test campaigns carried out at the NASA Ames Research Center 40-by-80-foot wind tunnel using the full-scale Bo 105 rotor (Ref. 17) and the same trim conditions. Correlations of rotor trim angles, rotor power and L/D_e are presented in Fig. 5. Additionally, the high-speed forward flight condition corresponding to Run 35 log-26 from Ref. 17 was used for structural loads validation and the results are shown in Fig. 6. Overall, the trends were correct and the magnitudes were sufficiently well predicted, giving confidence in the aeromechanics model for the succeeding comparative active rotor study.

Results and Discussion

In this work, the effect of different active rotor concepts on rotor power requirements was investigated. The results from a parametric study of morphing design and control variables are presented in the following. The primary focus was to obtain the dynamic and aerodynamic effects of the active camber mechanism. Additionally, IBC and active twist were used to compare the underlying aeroelastic effects that led to performance gains. The same modeling approach, numerical setup, and trim condition (see Table 1) were used throughout the entire investigation.

IBC and Active Twist

Since IBC is a full blade feathering mechanism, and 1P control is already provided via the swashplate, only 2P IBC actu-

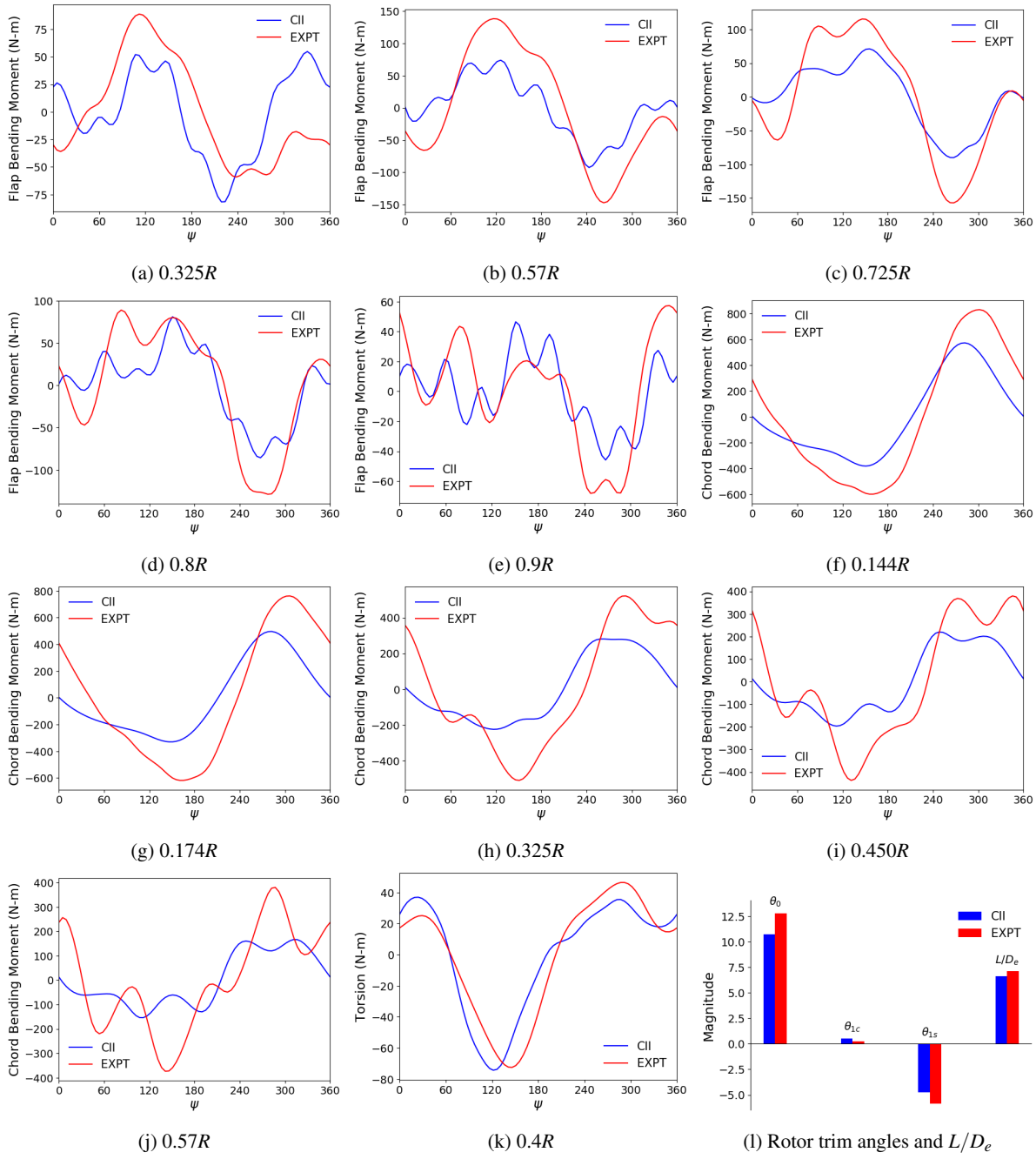

(a) 0.325R (b) 0.57R (c) 0.725R

(d) 0.8R (e) 0.9R (f) 0.144R

(g) 0.174R (h) 0.325R (i) 0.450R

(j) 0.57R (k) 0.4R (l) Rotor trim angles and L/D_e

Fig. 6. Correlation of measurement data with CAMRAD II results for trim condition of Table 1. (a)–(e) Oscillatory flap bending moment, (f)–(j) Oscillatory chord bending moment, (k) Oscillatory torsional moment, (l) Rotor control angles and L/D_e.

ation was studied. Optimal 1P active twist showed only minor performance improvements smaller than 0.4% compared to the baseline and is, therefore, not further discussed.

The effect of 2P IBC and 2P active twist control inputs on rotor power is shown in Fig. 7. The phase inputs shown are limited to the range that yielded most potential for performance improvement within the study. Figure 7a shows that IBC input of $A_{2P} = 1.25°$ and $\phi_{2P} = 95°$, referring to an increase of pitch angles at $\psi = 95°$ and $\psi = 275°$, resulted in rotor power reduction by about 1.8%. Figure 7b shows rotor power results corresponding to 2P active twist actuation. Here, $A_{2P} = 2.1°$ and $\phi_{2P} = 10°$, referring to an increased blade twist at $\psi = 10°$ and $\psi = 190°$, gave best rotor performance. The resulting power gain was similar to that obtained using IBC input.

Isolated 1P and 2P Active Camber Actuation

Considering potential design constraints, the active camber morphing section was limited to an outer edge location of

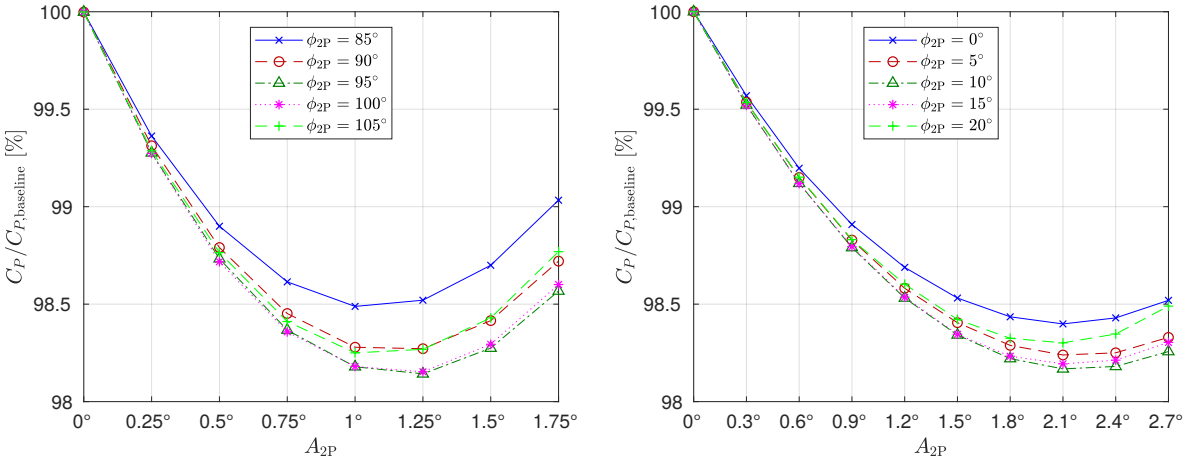

(a) IBC (b) active twist

Fig. 7. Rotor power improvements with 2P actuation for several phase angles.

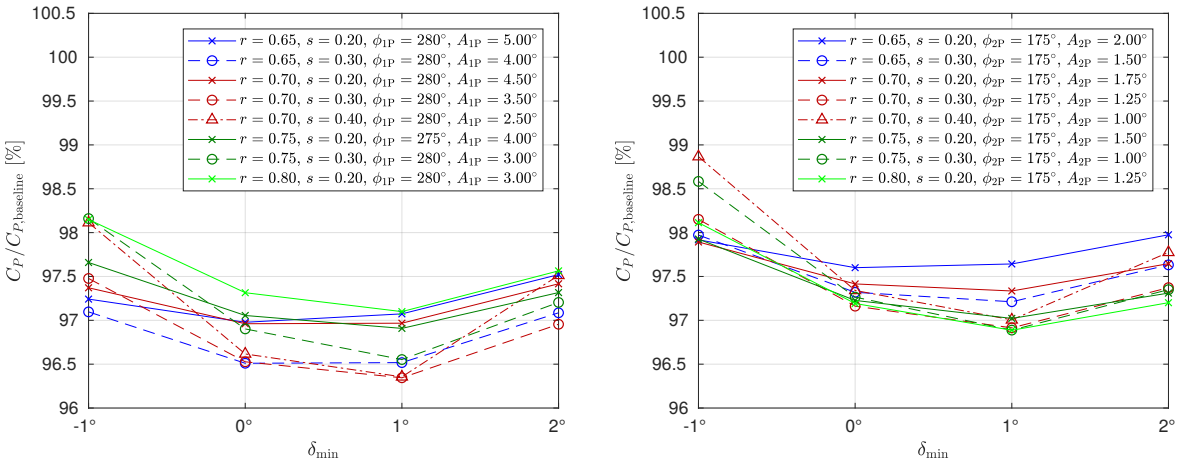

(a) 1P (b) 2P

Fig. 8. Effect of r, s and $\delta_{\min}$ on rotor power for the isolated active camber actuation.

0.9R. The inboard limit was set at 0.5R, since further inboard the dynamic pressure was deemed too low for the morphing section to be effective. The section length was varied between 0.1R and 0.4R with an increment of 0.1R. However, cases with the smallest section length, $s = 0.1$, did not yield comparable performance gains and are, therefore, not discussed in the following analysis. The actuation control subspace investigated in this study was based on preliminary results obtained as part of an earlier publication (Ref. 12). Table 2 details the range of design and control variables that were studied.

Based on a full-factorial study over the design space of Table 2, optimal control inputs, separately for 1P and 2P actuation, were identified for each geometric design configuration. Figures 8 to 10 show the dependence of rotor power on each of the control variables by perturbing them about the optimum. For example, 1P control inputs that resulted in optimal performance of a rotor with a morphing section of size $s = 0.2$ centered at $r = 0.65$ were $\delta_{\min} = 0°$, $\phi_{1P} = 280°$ and $A_{1P} = 5.0°$. To illustrate for $s = 0.2$ and $r = 0.65$ the effect of $\delta_{\min}$ variation, ϕ_{1P}, and A_{1P} values corresponding to the optimal inputs ($\phi_{1P} = 280°$ and $A_{1P} = 5.0°$) were retained.

Table 2. Design space for active camber study.

Variable		1P		2P	
		min	max	min	max
radial position (1/R)	r	0.65	0.8	0.65	0.8
radial length (1/R)	s	0.1	0.4	0.1	0.4
phase angle	ϕ_{nP}	250°	310°	160°	190°
minimum deflection	$\delta_{\min}$	-1°	2°	-1°	2°
amplitude	A_{nP}	0°	5.5°	0°	2.25°

Figure 8 shows the effect of minimum deflection angle $\delta_{\min}$ on rotor power. Considering the scheduling of actuation (see legend of Fig. 8 and Eq. 1), for both 1P and 2P actuation, the minimum deflection occurred close to $\psi = 90°$; for 2P actuation it additionally appeared close to $\psi = 270°$.A beneficial effect of this actuation scheduling is the low drag production of moderately cambered airfoils at high Mach numbers. Fo-

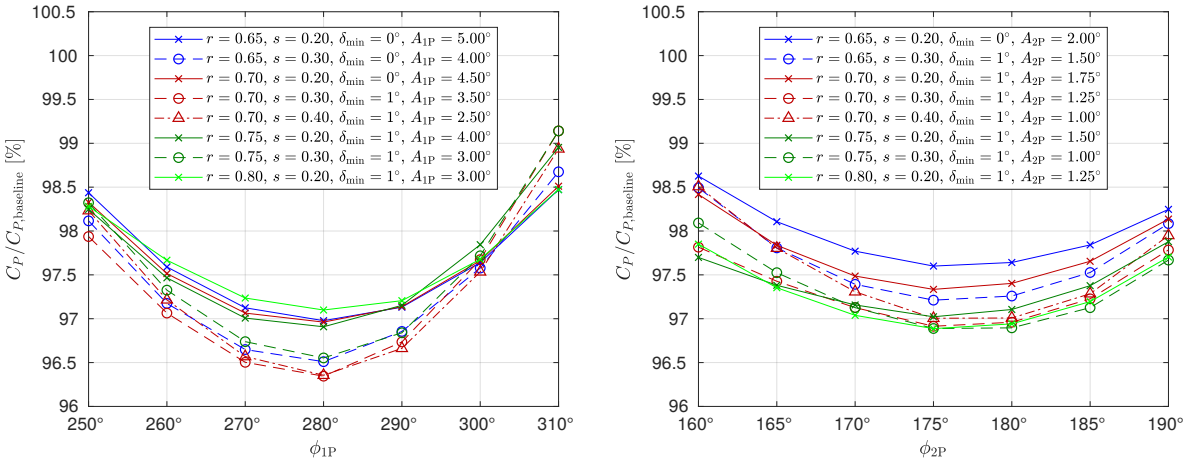

(a) 1P (b) 2P

Fig. 9. Effect of r, s and ϕ_{nP} on rotor power for the isolated active camber actuation.

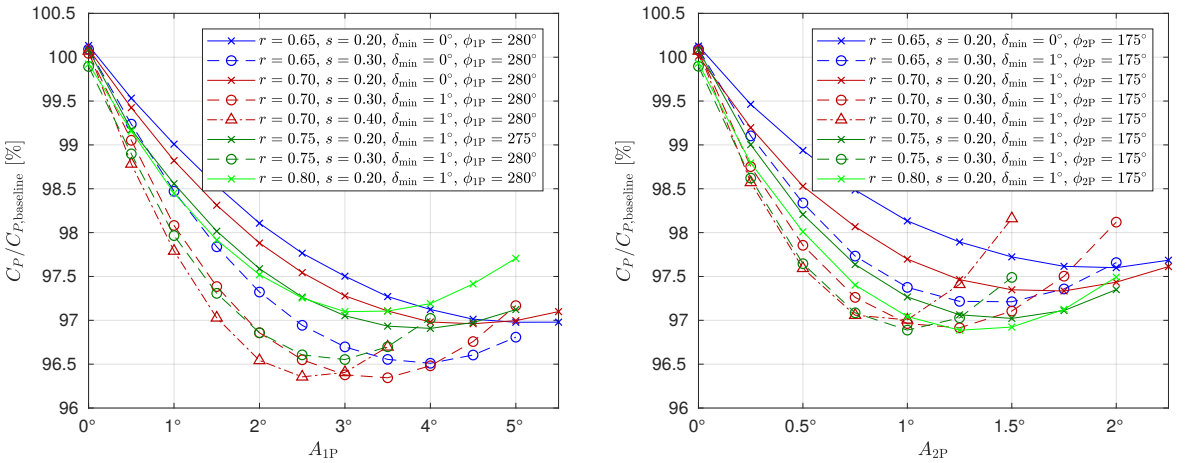

(a) 1P (b) 2P

Fig. 10. Effect of r, s and A_{nP} on rotor power for the isolated active camber actuation.

cusing on the optimum value for $\delta_{\min}$, a trend was observed that for both 1P and 2P actuation a $\delta_{\min}$ of approximately 1° was most favorable for all geometric design configurations studied. For morphing sections that lie inboard of $0.8R$, the optimum was shifted slightly towards $\delta_{\min} = 0°$. Overall, all investigated cases showed favorable mean camber deflections of $\delta_0 = \delta_{\min} + A_{\text{nP}}$ in the range of $2° - 6°$.

Based on Eq. 1, ϕ_{nP} results in an actuation profile with maximum deflection at $\psi = \phi_{\text{nP}}$ for actuation input at a single harmonic. For both 1P and 2P inputs, the optimal phasing was close to $\phi_{1P} = 280°$ and $\phi_{2P} = 175°$, respectively, independent of the geometric design parameters (see Fig. 9). Due to this behavior, the dependence on geometric design parameters can be seen most clearly in Fig. 9. Focusing on $\phi_{1P} = 280°$ in Fig. 9a, best performance was found with $r = 0.70$ and $s = 0.3$, corresponding to an active camber section ranging from $0.55R$ to $0.85R$. Although, the performance improvement obtained for $r = 0.70$, $s = 0.4$ was virtually identical. 2P actuation input resulted in optimal rotor performance for $\phi_{2P} = 175°$ (see Fig. 9b). The overall best performance gain obtained was identical for an active camber section from $0.7R$ to $0.9R$ and for $0.6R$ to $0.9R$. This outcome suggested that a further outboard positioning could potentially lead to greater power savings. However, this was not further investigated, because of expected blade integration difficulties further outboard. Due to its distinct differentiation against the optimum 1P case, for further analysis the configuration with $r = 0.80$ and $s = 0.2$ was chosen to be representative for the best 2P actuation case. Based on the results shown in Fig. 9, it can be concluded that radial location r of the morphing section had relatively less influence on rotor power at 1P actuation compared to 2P actuation. The opposite is true with regard to the influence of the morphing section size s. It had a greater effect on rotor power with 1P control input than with 2P input.

The influence of camber deflection amplitude, A_{1P} and A_{2P}, on the rotor power is illustrated in Fig. 10. For both actuation frequencies, the amplitude requirement increased with reduction of radial position and with greater length of the active camber

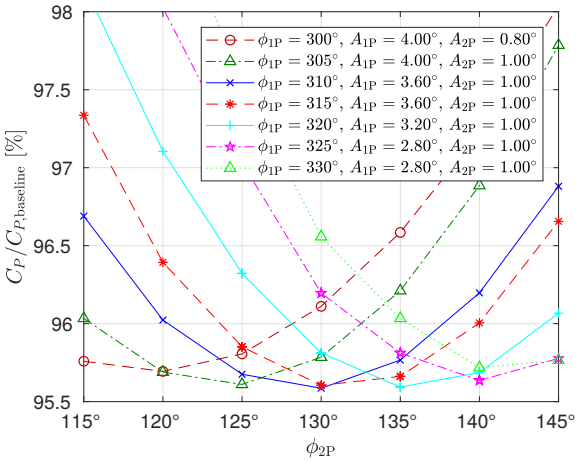

(a) $r = 0.7R,\ s = 0.4R$

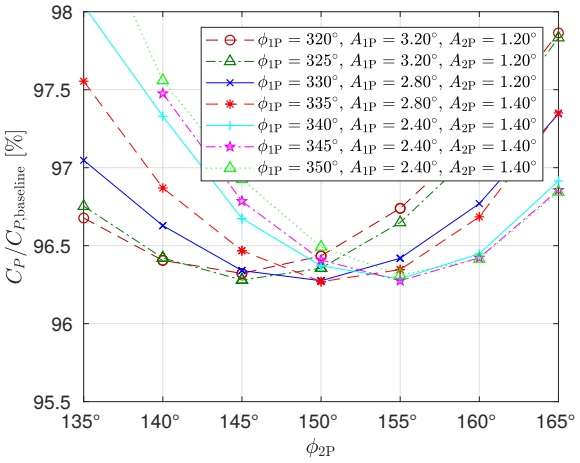

(b) $r = 0.8R,\ s = 0.2R$

Fig. 11. Effect of ϕ_{nP} on rotor power for $\delta_{min} = -1°$: 1P+2P actuation.

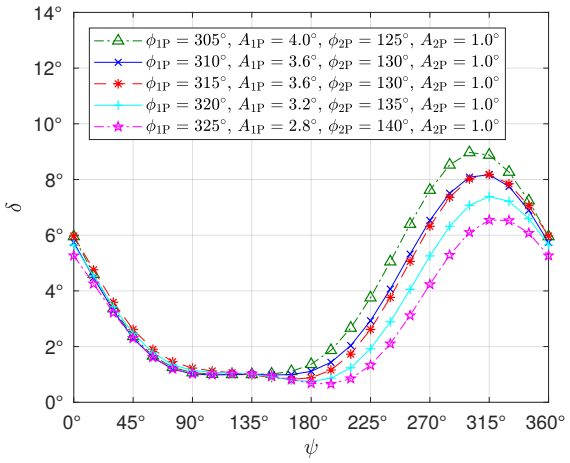

(a) $r = 0.7R,\ s = 0.4R$

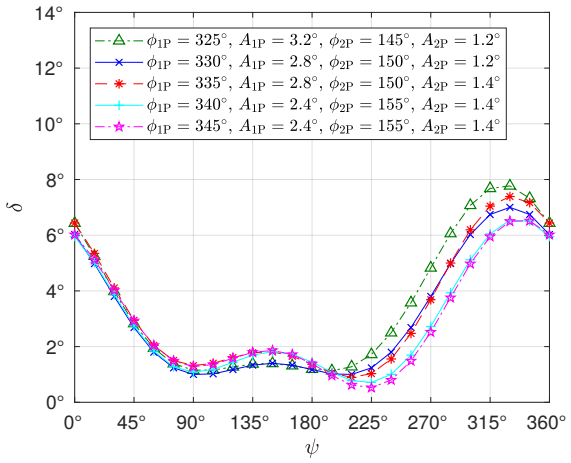

(b) $r = 0.8R,\ s = 0.2R$

Fig. 12. Actuation scheduling, corresponding to cases in Fig. 11.

section. Comparing 1P and 2P actuation, the optimal amplitudes were approximately in a relation of $A_{1P} = 2.5 \cdot A_{2P}$. Consequently, favorable actuation amplitudes covering the optima of all investigated geometric configurations ranged from 1° to 5°. Best performance improvement in the isolated study was obtained with an actuation amplitude of $A_{1P} = 3.5°$, referring to a deflection between $\delta = 1°$ and $\delta = 8°$.

Overall, with 1P actuation a greater performance gain over the baseline was observed (3.6%) than with 2P actuation (3.1%). Both results, however, were significantly greater than those obtained by IBC or active twist, which were in the order of 1.8%.

Superimposed 1P+2P Active Camber Actuation

To investigate the influence of a combined actuation of 1P and 2P harmonics, a full-factorial study of the combined design space of 1P and 2P actuation was conducted. To capture all relevant trends, a finer resolution in the control parameter sweep through the design space was adopted, resulting in over 40,000 cases. The cases with the smallest morphing section $s = 0.1$ were excluded from this study, because they did not give performance improvements.

The isolated harmonic input study showed that the optimal phasing was nearly independent of every other design and control variable (see Fig. 9). For the superimposed 1P+2P study, it was found that the combination of ϕ_{1P} and ϕ_{2P} that led to optimal performance had a relatively complex dependence on A_{1P} and A_{2P}, which, in turn, depended on r, s and δ_{min}. As a result, it was more difficult to obtain clear trends indicating the effect of the active camber section design and control variables on overall rotor power.

To understand the complex relation between 1P and 2P phasing, two different geometric design configurations, [$r = 0.7$, $s = 0.4$] and [$r = 0.8$, $s = 0.2$], were analyzed and the results are shown in Fig. 11. Values of the control variables ϕ_{1P}, ϕ_{2P}, A_{1P}, and A_{2P} were chosen such that the resulting performance

gain was close to the optimal gain possible corresponding to each geometric design configuration. A perturbation study of ϕ_{1P} and ϕ_{2P} revealed that optimal performance was possible over a much broader range of ϕ_{nP}, unlike in the isolated harmonic input case. Figure 12 shows that these control parameters resulted in actuation profiles that were nearly identical on the advancing side of the rotor disk. Even on the retreating side, all of the actuation profiles had similar form and differed only in the magnitude of peak deflection.

In Fig. 11a, the overall best ϕ_{1P} was determined to be 310°, while $\phi_{1P} = 320°$ still resulted in a better result than $\phi_{1P} = 315°$. This discontinuity indicated an insufficient step size of ϕ_{2P}, however, with insignificant impact on the optimum rotor performance. In contrast, significant was the effect of using combinations of ϕ_{1P} and ϕ_{2P} where ϕ_{2P} did not correspond to the optimal complement of ϕ_{1P}.

From Fig. 11b it appeared that a different geometric design configuration ($r = 0.8$, $s = 0.2$) compared to that in Fig. 11a showed very similar trends, although for different actuation profiles. Here, the best case was found using $\phi_{1P} = 335°$ and $\phi_{2P} = 150°$, $A_{1P} = 2.80°$, and A_{2P} from 1.20°. However, comparing it to the best case obtained with $\phi_{1P} = 330°$, an insignificant change in rotor power improvement, but a notable decrease of A_{2P} from 1.20° to 1.40° was obtained. This discontinuity indicated an insufficiently small amplitude step size, however, irrelevant to the overall result. The corresponding camber deflection in Fig. 12b illustrates that the actuation schemes along ψ were comparable to the case with $r = 0.7$ and $s = 0.4$ (see Fig. 12a), however, shaped more evidently by a 2P characteristic.

Figure 13 shows the influence of δ_{min} on rotor power. Figure 13a illustrates the global influence of δ_{min} on rotor power, using optimal control inputs for each design configuration and δ_{min} within the range of $-1°$ to $1°$. A global extremum was established for $r = 0.7$ and $s = 0.4$ with $\delta_{min} = -1°$ by extending the range of δ_{min} investigation to include $-2°$. Although corresponding extrema could not established for all design configurations, it was decided that due to the low gradient of $C_P - \delta_{min}$-curves the added computational expense was not justified and $\delta_{min} = -1°$ was adopted for all design configurations. The control settings, for $\delta_{min} = -1°$, that led to optimal performance corresponding to each design configuration are specified in Table 3. A perturbation analysis of δ_{min} in Fig. 13b shows the sensitivity of rotor power on δ_{min}, based on control settings from Table 3. This suggests that when changing δ°_{min}, all control settings have to be adjusted accordingly (see Fig. 13a) to preserve the amount of performance improvement.

Figure 14 corresponds to Fig. 11, showing the result in less detail, but for all geometric design configurations. In Fig. 14a, the range of optimal phasing varied between 300° and 335° depending on the morphing section size. Particularly for small camber sections, a great dependence on radial placement r existed. The range of ϕ_{2P} values leading to optimal rotor power was between 130° and 150° (see Fig. 14b). Again, the dependence on r was significant, however, with an inflection point at $r = 0.70$. In this case, for larger as well as for smaller radial stations, an increase in phasing was required. In general, superimposed 1P+2P actuation resulted in an increase of 1P phasing and a reduction of 2P phasing compared to the isolated harmonic actuation. Further inboard placed active camber sections showed favorable combinations of 1P and 2P phasing, which were slightly shifted towards the best ϕ_{1P} from the isolated study, while ϕ_{2P} diverged from the optimal isolated 2P phasing. Further outboard placement showed the contrary trend.

Table 3. Optima for each geometric design that was studied using $\delta_{min} = -1°$.

r	s	δ_{min}	ϕ_{1P}	A_{1P}	ϕ_{2P}	A_{2P}
0.65	0.20	$-1°$	305°	4.80°	140°	1.20°
0.65	0.30	$-1°$	305°	4.40°	130°	1.00°
0.70	0.20	$-1°$	305°	4.80°	135°	1.20°
0.70	0.30	$-1°$	305°	4.00°	130°	1.00°
0.70	0.40	$-1°$	310°	3.60°	130°	1.00°
0.75	0.20	$-1°$	320°	3.60°	145°	1.40°
0.75	0.30	$-1°$	320°	3.20°	140°	1.00°
0.80	0.20	$-1°$	335°	2.80°	150°	1.40°

The influence obtained from a variation of 1P amplitude (see Fig. 15a) was similar to that obtained in the isolated study. In general, with a further outboard placement and longer radial extension the amplitude requirement was lower. This, in particular, was visible when analyzing the shift in position from $r = 0.70$ to $r = 0.75$ using an active camber section with $s = 0.3$. Hereby, a step in optimal actuation amplitude from 4° to 3.2° was observed, without majorly affecting the power improvement. The effect of A_{2P} on rotor power was less dependent on design parameters (see Fig. 15b). For $s > 0.2$, all configurations yielded an optimum close to $A_{2P} = 1°$. This can be explained by the compensation of two contrary effects: With an increase in radial station the contribution of 2P actuation had to increase to produce best rotor performance. However, with further outboard placement a reduction in amplitude requirement was generally observed. Thus, in total, the amplitude requirement remained nearly constant. Neither most outboard nor most inboard radial stations showed best efficiency. Hence, a predefined radial limitation of active camber application to the blade between $0.5R$ and $0.9R$ did not significantly influence the obtained performance improvement.

Analysis of Active Rotor Dynamics and Aerodynamics

The effect of optimal active rotor design and control inputs on rotor dynamics and aerodynamics is shown in Figs. 16 to 20, for the settings summarized in Table 4. Figure 17 illustrates the deflection scheduling corresponding to optimal active camber actuation cases in Table 4.

Conforming to rotor physics during high-speed forward flight, Fig. 16a shows high thrust contributions from the front and the aft regions of the rotor disk for the baseline rotor. The blade tips were negatively loaded on the advancing side due to negative angles of attack as a result of high induced twist. Op-

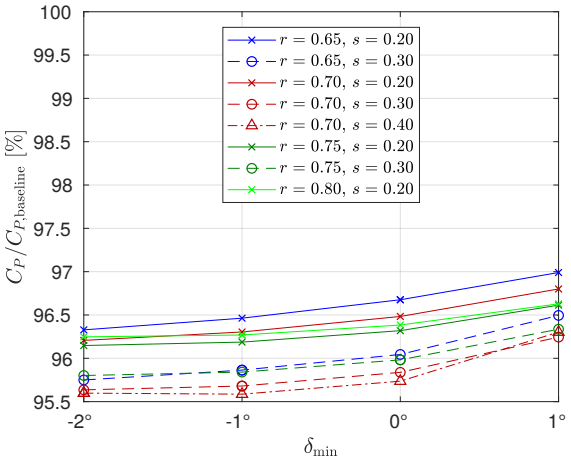

(a) Optimal control settings for each $\delta_{\min}$.

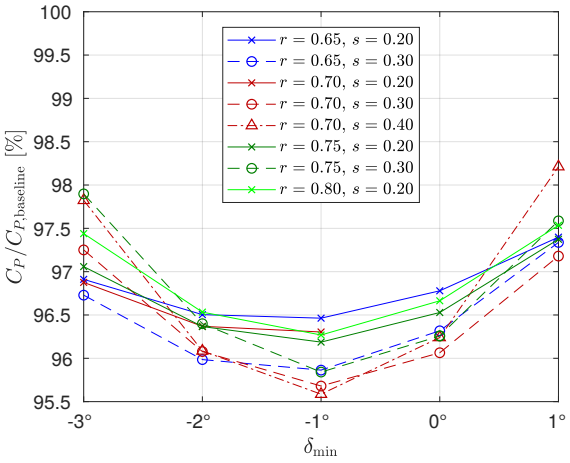

(b) Constant control settings (except for $\delta_{\min}$) based on Table 3

Fig. 13. Effect of r, s and $\delta_{\min}$ on rotor power for 1P+2P actuation.

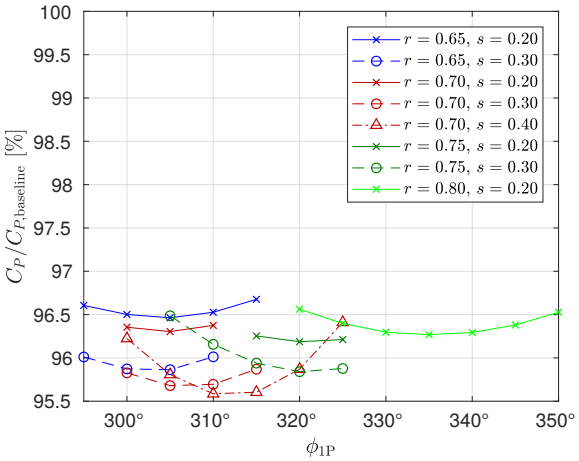

(a) ϕ_{1P}

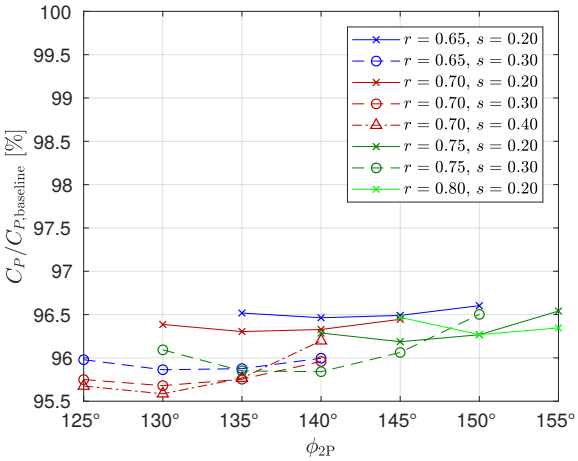

(b) ϕ_{2P}

Fig. 14. Effect of r, s and ϕ_{nP} on rotor power for 1P+2P actuation based on settings from Table 3.

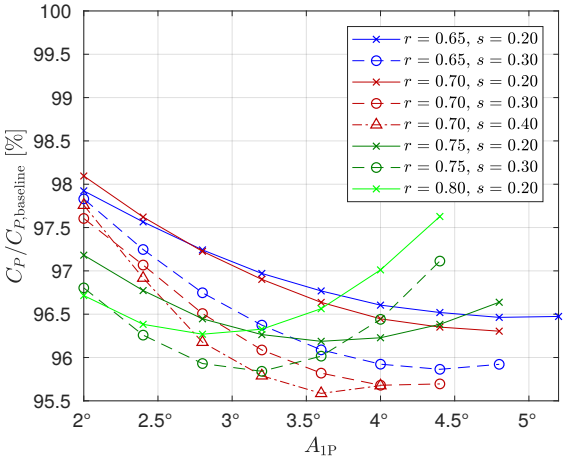

(a) A_{1P}

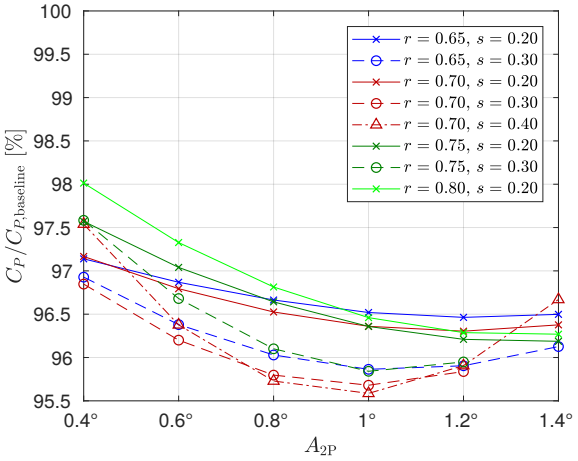

(b) A_{2P}

Fig. 15. Effect of r, s and A_{nP} on rotor power for 1P+2P actuation based on settings from Table 3.

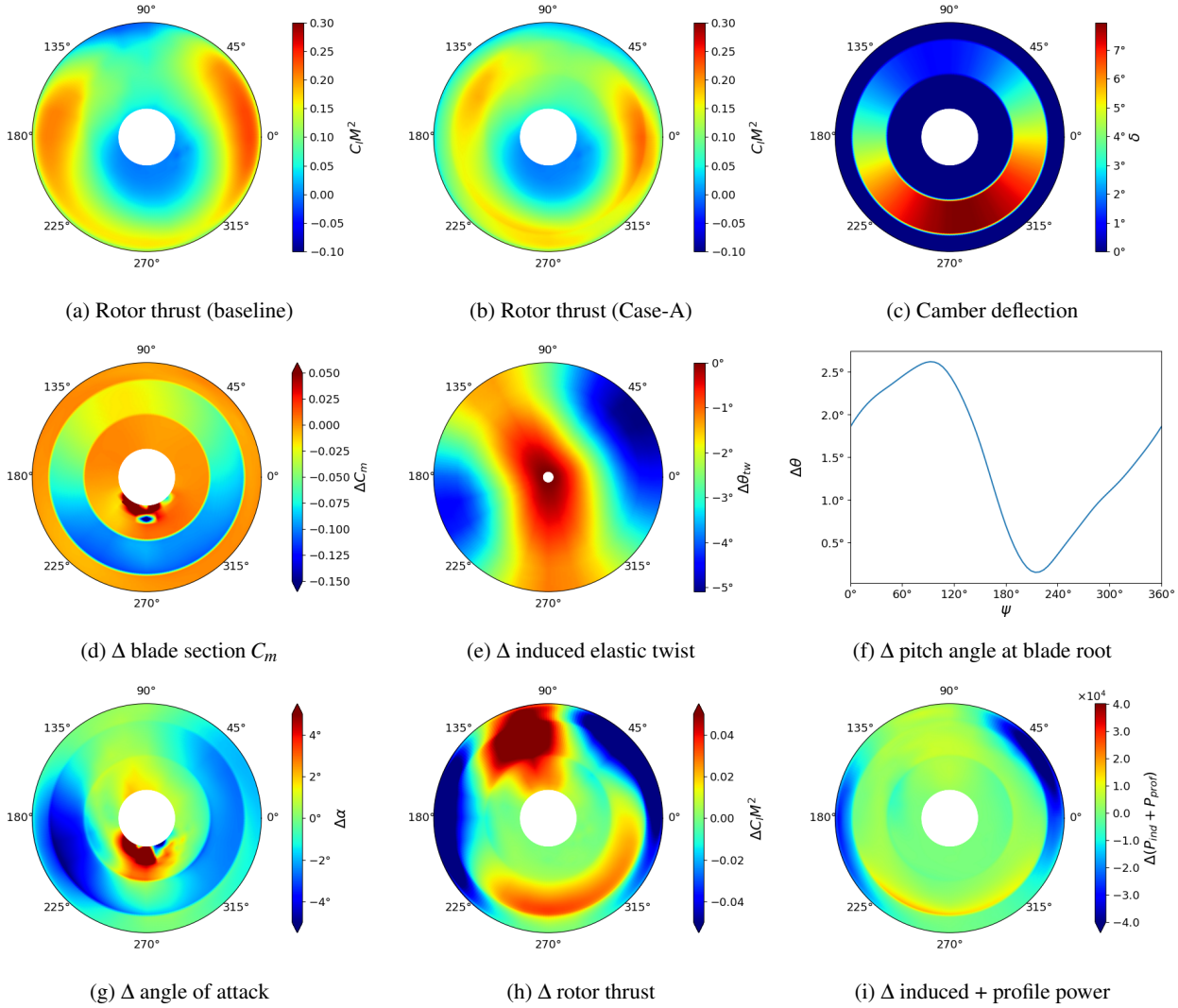

(a) Rotor thrust (baseline)

(b) Rotor thrust (Case-A)

(c) Camber deflection

(d) Δ blade section C_m

(e) Δ induced elastic twist

(f) Δ pitch angle at blade root

(g) Δ angle of attack

(h) Δ rotor thrust

(i) Δ induced + profile power

Fig. 16. Polar plots illustrating the effect of active camber actuation Case-A (optimal 1P) and the change (over non-morphing baseline) in rotor structural and aerodynamic parameters, showing baseline thrust distribution as a reference.

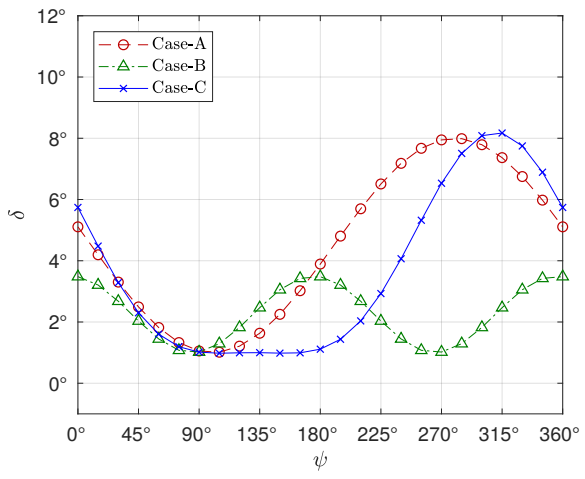

Fig. 17. Actuation scheduling along the azimuth; $r = 0.7$ and $s = 0.4$; optima for 1P, 2P and 1P+2P actuation ($\delta_{\min} = -1°$).

Table 4. Optimal active rotor actuation, A: 1P active camber, B: 2P active camber, C: 1P+2P active camber, D: IBC, E: active twist.

Case	r	s	$\delta_{\min}$	ϕ_{1P}	A_{1P}	ϕ_{2P}	A_{2P}
A	0.70	0.30	1°	280°	3.50°	0°	0.00°
B	0.80	0.20	1°	0°	0.00°	175°	1.25°
C	0.70	0.40	−1°	310°	3.60°	130°	1.00°
D	–	–	–	–	–	95°	1.25°
E	–	–	–	–	–	10°	2.10°

timal performance gain with 1P actuation resulted from maximum camber deflection at $\psi = 280°$ (see Fig. 16c). Since the active camber section had a positive deflection throughout its actuation cycle (because $\delta_{\min} = 1°$), the increased camber induced a negative torsional moment over the entire azimuth (see Fig. 16d). Therefore, the blade elastic twist increased over the entire disk (see Fig. 16e). Figure 16f shows that trimming the morphing rotor to the same flight condition as the

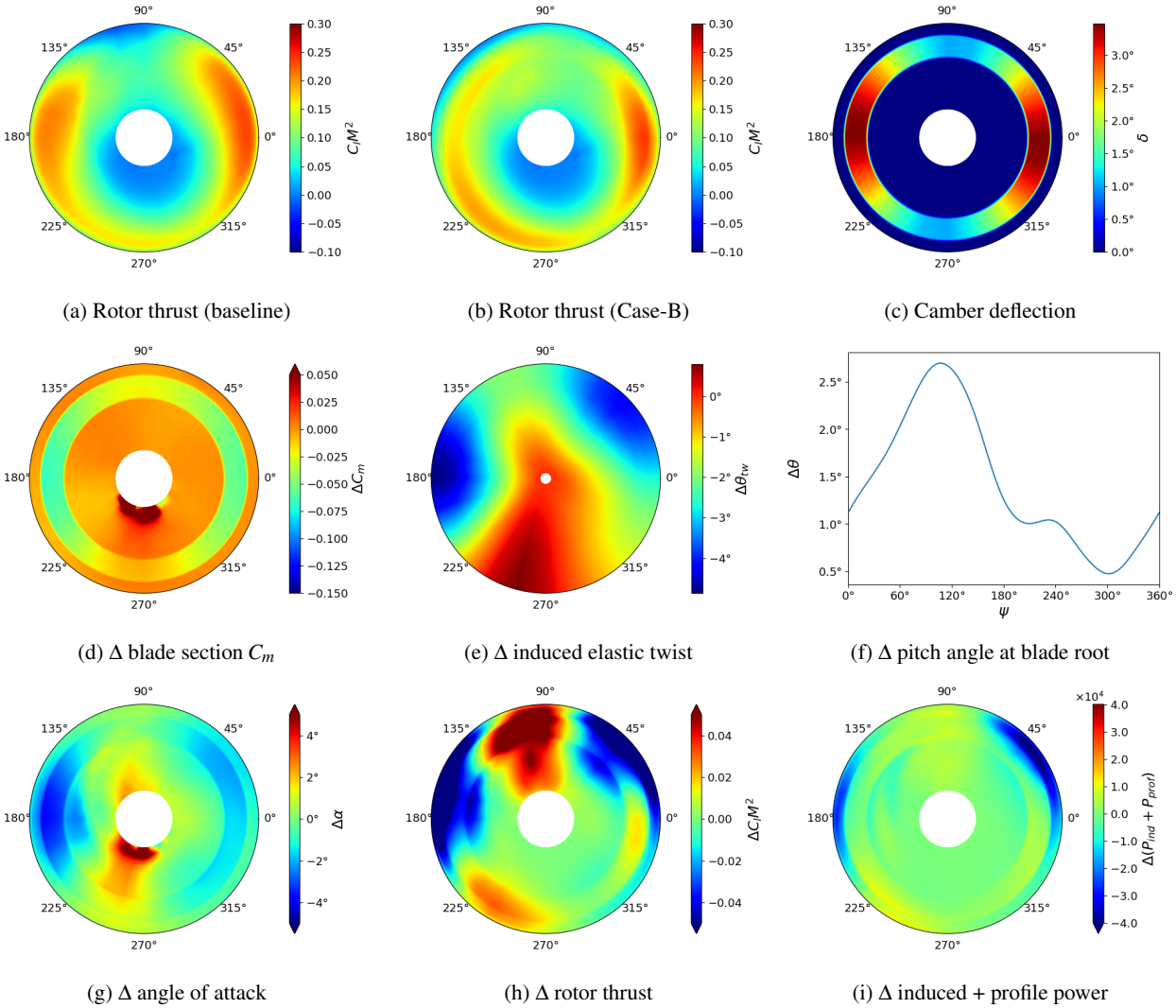

(a) Rotor thrust (baseline)

(b) Rotor thrust (Case-B)

(c) Camber deflection

(d) Δ blade section C_m

(e) Δ induced elastic twist

(f) Δ pitch angle at blade root

(g) Δ angle of attack

(h) Δ rotor thrust

(i) Δ induced + profile power

Fig. 18. Polar plots illustrating the effect of active camber actuation Case-B (optimal 2P) and the change (over non-morphing baseline) in rotor structural and aerodynamic parameters, showing baseline thrust distribution as a reference.

baseline rotor resulted in a higher pitch at the blade root over the entire azimuth. The overall effect was a small increase in angle of attack on the advancing side, and a notable decrease at the front and aft of the rotor disk (see Fig. 16g). The retreating side showed little change in angle of attack. However, the rotor thrust also increased on the retreating side due to high camber deflection. This resulted in increased loading on the lateral sides of the rotor disk and a decrease over the front and aft sections (see Fig. 16h). Thus, a more uniform distribution of thrust over the rotor disk was apparent when comparing Figs. 16a and 16b. Additionally, the thrust was reduced in regions of the rotor disk far outboard and increased in regions further inboard in comparison to the baseline (see Fig. 16h), which also affected the induced rotor power. Finally, Fig. 16i shows the local effects of 1P active camber deflection on rotor power.

Despite the differences in their deflection scheduling (see Fig. 17), optimal 2P and superimposed 1P+2P active camber actuation both had a similar effect on rotor structural dynamics and aerodynamics as 1P input (see Figs. 18 and 19). Yielding to the induced torsional moment, elastic blade twist increased almost over the entire rotor disk. The change in the angle of attack distribution, as a result of trimming the rotor to the same trim targets, resulted in a more uniform thrust distribution over the rotor disk.

Figure 20 shows that both IBC and active twist actuation reduced the thrust concentration at the front and aft sections of the rotor disk. Increased loading at the retreating side allowed the negative loading at the blade tip of the advancing side to be alleviated while maintaining roll moment balance. However, in contrast to the 1P and superimposed 1P+2P active camber actuation, the redistribution of thrust towards more inboard sections was less apparent.

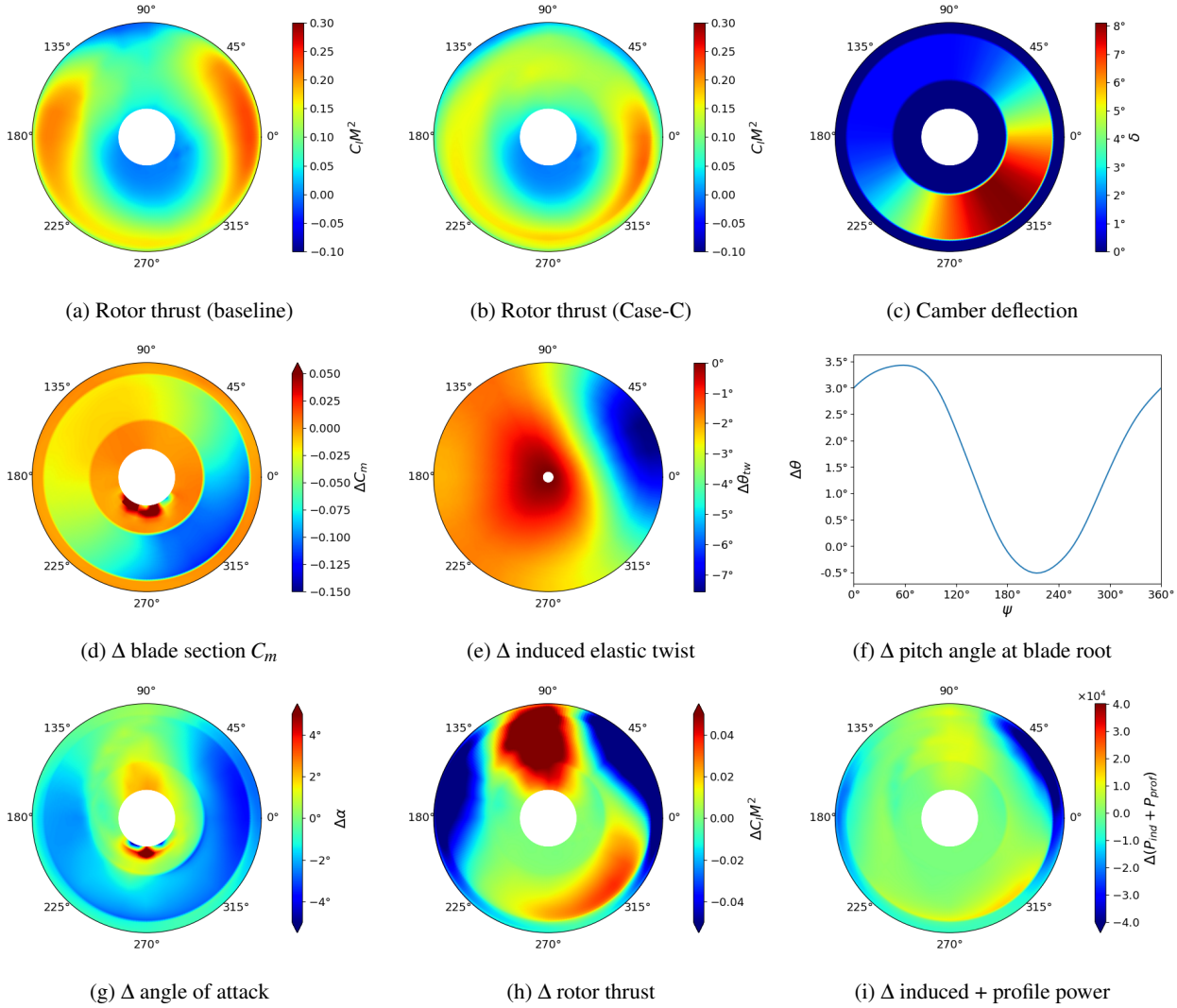

(a) Rotor thrust (baseline)

(b) Rotor thrust (Case-C)

(c) Camber deflection

(d) Δ blade section C_m

(e) Δ induced elastic twist

(f) Δ pitch angle at blade root

(g) Δ angle of attack

(h) Δ rotor thrust

(i) Δ induced + profile power

Fig. 19. Polar plots illustrating the effect of active camber actuation Case-C (optimal 1P+2P) and the change (over non-morphing baseline) in rotor structural and aerodynamic parameters, showing baseline thrust distribution as a reference.

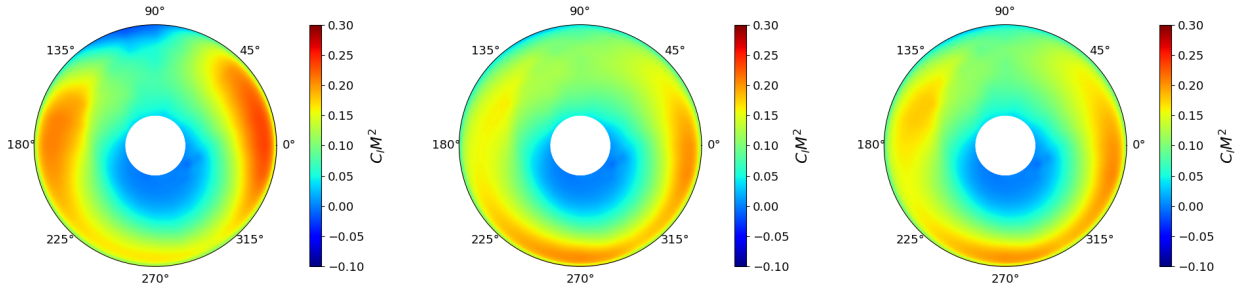

(a) Baseline

(b) 2P IBC (Case-D)

(c) 2P active twist (Case-E)

Fig. 20. Polar plots illustrating the non-dimensional rotor thrust distribution of the baseline and induced due to optimal IBC and active twist actuation.

Conclusions

In the present study, the application of active camber was investigated numerically to identify optimal geometric design and control to maximize rotor power improvements in fast forward flight. The investigation was conducted with the comprehensive rotor analysis code CAMRAD II, that was used to model an isolated full-scale Bo 105 rotor that was used as the baseline rotor. The active camber morphing mechanism was implemented on this rotor. An extensive range of actuation control inputs was evaluated for multiple radial locations and spanwise section lengths of the active camber mechanism. Isolated 1P and 2P actuation, and superimposed 1P+2P control inputs were analyzed and compared to optimal results obtained from 2P IBC and 2P active twist actuation, based on the same modeling approach.

With active camber actuation, significant performance improvements were observed, clearly outperforming the results of active twist and IBC. The overall best rotor power improvements (over the baseline) observed for the investigated active rotor concepts were:

1. IBC: 1.8%; Active twist: 1.8%
2. Active camber, isolated study actuated with 1P: 3.6%; actuated with 2P: 3.1%
3. Active camber, superimposed 1P+2P actuation: 4.4%

The performance improvements from using active camber morphing resulted from improved sectional aerodynamics and from a more uniform distribution of the thrust over the rotor disk. The peaks in disk loading in the front and aft regions of the rotor disk were attenuated and the advancing and retreating sides were increasingly loaded. Moreover, regions on the rotor disk that revealed highest loads moved radially inboard causing a reduction in induced rotor power. These effects were achieved by a combination of induced elastic blade twist, caused by an increased C_m of the morphed camber section, and a resulting adjustment of the blade pitch from swashplate control to maintain the trim targets.

Maximum performance improvements (i.e., power savings) were achieved by the following combinations of geometric design and control input parameters.

1. A spanwise active camber section length of $s = 0.1$ was not efficient compared to section lengths of $s > 0.1$. With 2P actuation, the optimum did not significantly change by increasing $s > 0.2$. Using 1P actuation, an active camber section length of $s = 0.3$ resulted in greater rotor performance gains than $s < 0.3$. A further increase of s affected the rotor power improvement insignificantly. Superposition of 1P and 2P actuation showed maximum power savings using the longest active camber section of $s = 0.4$.
2. The best 1P actuation case was observed with $r = 0.70$, $s = 0.3$, $\delta_{\min} = 1^\circ$, $\phi_{1P} = 280^\circ$, and $A_{1P} = 3.5^\circ$.
3. With 2P actuation, two geometric configurations led to similar performance improvements. A combination of $r = 0.80$ and $s = 0.2$, actuated with $\delta_{\min} = 1^\circ$, $\phi_{2P} = 175^\circ$ and $A_{2P} = 1.25^\circ$, and a configuration with $r = 0.75$, $s = 0.3$ actuated with $\delta_{\min} = 1^\circ$, $\phi_{2P} = 175^\circ$, and $A_{2P} = 1.00^\circ$.
4. A superposition of 1P and 2P actuation yielded the overall best performance, using $r = 0.70$ and $s = 0.4$, $\delta_{\min} = -1^\circ$, $\phi_{1P} = 310^\circ$, $A_{1P} = 3.6^\circ$, $\phi_{2P} = 130^\circ$, and $A_{2P} = 1.0^\circ$.

In the superimposed 1P+2P study, a considerable variation and combination of design parameters led to almost identical performance improvements compared to the global optimum of the study. This outcome provides certain flexibility in the design of such a mechanism, which may be limited by manufacturing or blade integration challenges. Furthermore, it leaves room for additional optimization targets such as acoustics, vibrations, loads and actuation power requirements, which shall be addressed within the continuation of this project by a multi-objective optimization.

Author contact:

Dominik Komp: dominik.komp@tum.de

Sumeet Kumar: sumeet.kumar@tum.de

Amine Abdelmoula: amine.abdelmoula@tum.de

Manfred Hajek: hajek@tum.de

Jürgen Rauleder: juergen.rauleder@tum.de

Acknowledgments

This project has received funding from the European Union's Horizon 2020 research and innovation program under grant agreement No. 723491.

References

[1]Yeo, H., "Assessment of Active Controls for Rotor Performance Enhancement," *Journal of the American Helicopter Society*, Vol. 53, (2), 2008.
doi: 10.4050/JAHS.53.152

[2]Jain, R., Yeo, H., and Chopra, I., "Computational Fluid Dynamics – Computational Structural Dynamics Analysis of Active Control of Helicopter Rotor for Performance Improvement," *Journal of the American Helicopter Society*, Vol. 55, (4), 2010.
doi: 10.4050/JAHS.55.042004

[3]Jain, R., Yeo, H., and Chopra, I., "Examination of Rotor Loads Due to On-Blade Active Controls for Performance Enhancement," *Journal of Aircraft*, Vol. 47, (6), 2010, pp. 2049–2066.
doi: 10.2514/1.C000306

[4]Ravichandran, K., Chopra, I., Wake, B. E., and Hein, B., "Trailing-Edge Flaps for Rotor Performance Enhancement and Vibration Reduction," *Journal of the American Helicopter Society*, Vol. 58, (2), April 2013.
doi: 10.4050/JAHS.58.022006

[5]Liu, L., Friedmann, P. P., Kim, I., and Bernstein, D. S., "Rotor Performance Enhancement and Vibration Reduction in Presence of Dynamic Stall Using Actively Controlled Flaps," *Journal of the American Helicopter Society*, Vol. 53, (4), 2008, pp. 338–350.
doi: 10.4050/JAHS.53.338

[6]Jacklin, S. A., Blass, A., Swanson, S. M., and Teves, D., "Second Test of a Helicopter Individual Blade Control System in the NASA Ames 40- by 80-Foot Wind Tunnel"," American Helicopter Society 2nd International Aeromechanics Specialists Conference, Bridgeport, CT, October 1995.

[7]Yeo, H., Romander, E. A., and Norman, T. R., "Investigation of Rotor Performance and Loads of a UH-60A Individual Blade Control System," *Journal of the American Helicopter Society*, Vol. 56, (4), 2011, pp. 1–18.
doi: 10.4050/JAHS.56.042006

[8]Celi, R. and Cheng, R. P., "Optimum Two-Per-Revolution Inputs for Improved Rotor Performance," *Journal of Aircraft*, Vol. 42, (6), 2005, pp. 1409–1417.
doi: 10.2514/1.20884

[9]Jacklin, S. A., Nguyen, K. Q., Blass, A., and Richter, P., "Full-Scale Wind Tunnel Test of a Helicopter Individual Blade Control System," 50th Annual Forum of the American Helicopter Society, Washington, DC, May 1994.

[10]Woods, B. K., Bilgen, O., and Friswell, M. I., "Wind Tunnel Testing of the Fish Bone Active Camber Morphing Concept," *Journal of Intelligent Material Systems and Structures*, Vol. 25, (7), 2014, pp. 772–785.
doi: 10.1177/1045389X14521700

[11]Jain, R., Yeo, H., and Chopra, I., "Investigation of Trailing-Edge Flap Gap Effects on Rotor Performance Using High Fidelity Analysis," *Journal of Aircraft*, Vol. 50, (1), 2012, pp. 140–151.
doi: 10.2514/1.C031837

[12]Rauleder, J., van der Wall, B. G., Abdelmoula, A., Komp, D., Kumar, S., Ondra, V., Titurus, B., and Woods, B. K. S., "Aerodynamic Performance of Morphing Blades and Rotor Systems," American Helicopter Society 74th Annual Forum, Phoenix, AZ, May 2018.

[13]Johnson, W., "Technology Drivers in the Development of CAMRAD II," American Helicopter Society Aeromechanics Specialists Conference, San Francisco, CA, January 1994.

[14]Schwamborn, D., Gerhold, T., and Hannemann, V., "On the Validation of the DLR-TAU Code," *New Results in Numerical and Experimental Fluid Mechanics II*, Springer, 1999, pp. 426–433.

[15]Abdelmoula, A. and Rauleder, J., "Aerodynamic Performance of Morphed Camber Rotor Airfoils," AIAA Scitech 2019 Forum, January 2019.
doi: 10.2514/6.2019-1101

[16]Johnson, W., *Rotorcraft Aeromechanics*, Cambridge University Press, 2013.

[17]Peterson, R. L., Maier, T. H., Langer, H. J., and Tränapp, N., "Correlation of Wind Tunnel and Flight Test Results of a Full-Scale Hingeless Rotor," American Helicopter Society Aeromechanics Specialist Conference, San Francisco, CA, January 1994.

[18]Langer, H., Tränapp, N., and Deutsche Forschungsanstalt fuer Luft-und Raumfahrt eV (DLR), B. G. I. f. F., "BO105 Flight Test Data for a Wind Tunnel Test Program," *DLR IB*, 1993, pp. 111–93.